Analysis of the magnetic properties of core-shell iron oxide nanoparticles

F.A. Cholico[a], A.H. Sámano[a], R. Castañeda-Priego[c], J.A. Paz[a], L.H. Quintero[b] and M. E. Cano[a,*]

[a]*Centro Universitario de la Ciénega, Universidad de Guadalajara,*
Av. Universidad, 1115, Ocotlan, JAL, 47820, Mexico.
[*]*e-mail: eduardo.cano@cuci.udg.mx, Phone: 52-392 925 9400.*
[b]*Centro Universitario de Ciencias Económico Administrativas, Universidad de Guadalajara,*
Periférico Norte 799, Col. Los Belenes Ocotlán, C.P 45100, Zapopan, Jalisco, Mexico.
[c]*Departamento de Ingeniería Física, División de Ciencias e Ingenierías, Universidad de Guanajuato,*
Loma del bosque 103, Col. Lomas del Campestre, 37150, León, Gto. Mexico.

Received 9 December 2021; accepted 7 February 2022

We report on the magnetization of core-shells nanoparticles. Magnetic nanoparticles (MNPs) with a core of magnetite of 13 nm diameter covered with a shell of dopamine (1.1 nm thickness) are studied through vibrating sample magnetometer (VSM), Monte Carlo (MC) computer simulations, and using an analytical model. All parameters involved in the theoretical analysis are experimentally determined, namely, the magnetic moment, temperature, magnetic field, core diameter, shell thickness, magnetic anisotropy, and particle concentration. The dependence of the magnetization with the magnetic field obtained through VSM and MC shows a 1% discrepancy in the magnetic saturation and up to 40% in the initial magnetic susceptibility. However, the dependence of the magnetization with the temperature obtained by MC indicates that the MNPs obey the Curie law above a critical temperature of 100 K. Furthermore, our findings indicate that the dipolar interactions play an important role on the magnetization in the interval $20 < T < 100$ K. That critical temperature domain is very close to the blocking temperature measured following the zero-field-cooled and zero-cooled protocols, where the dipolar interactions between MNPs become significant. Further analysis shows a Langevin-like behavior for both experimental and theoretical magnetizations.

Keywords: Dopamine; nanoparticle; magnetization; core-shell.

DOI: https://doi.org/10.31349/RevMexFis.68.041004

1. Introduction

The development of new magnetic nanomaterials has gained much importance due to their novel applications in several disciplines, mainly those related to biomedical applications [1].

Currently, iron oxide magnetic nanoparticles (MNPs) of magnetite are manufactured following various chemical methods [2,3], obtaining beads with spherical shape and core-shell structures, which have high magnetic saturation, low hysteresis, and good biocompatibility with cell cultures [1,4]. The theoretical modeling of the MNPs allows us to study the magnetic behavior of these nanomaterials under different thermodynamic conditions, also to quantify the interaction between nanoparticles to determine the magnetic anisotropic effects involved [5].

The ferrimagnetic behavior of magnetite and a lot of ferrites was widely explained by Louis Néel during the 20th century. In magnetite, this response is caused by the tetrahedral and octahedral overlapped sublattices of the ions Fe3+ and Fe2+/Fe3+, which are located in the interstitial places of the crystalline structure FCC formed by the oxygen atoms, where the antiparallel orientation of the magnetic moments are arranged as an "antiferromagnetic imperfect ordering [6]". The antiferromagnetic and ferrimagnetic orderings depend on the temperature T and both disappear above a critical temperature T_N or T_C (called Néel or Curie temperature, respectively), reaching a paramagnetic behavior [6,7].

Monte Carlo (MC) computer simulations are a useful alternative to complement the analysis of the magnetic properties of the MNPs; several works have modeled the magnetization M of antiferromagnetic systems based on iron oxides (or magnetic systems in general) employing the Ising model [8-10]. Other works have used MC computer simulations with similar purposes, but using an oversimplified model, which considers a fluid of magnetic hard spheres (MHS) or discs, which are influenced by a magnetic field of magnitude H [11,12].

The main aim of this work is to study both experimentally and theoretically the magnetization (M) behavior of magnetic core-shell spheres (CSS), with a particular interest in CSS of magnetite coated with dopamine. This type of nanoparticles has been probed successfully *in vitro* and *in vivo* experiments of magnetic hyperthermia. The molecular approach here considered to carry out MC computer simulations is explicitly built with the measured parameters of the CSS, such as the diameter of the magnetic core, thickness of the coating, magnetic moment, concentration of MNPs, magnetic field, anisotropy constant, and temperature. Later, the computed magnetization dependences M *vs* H and M *vs* T are analyzed and compared with those obtained using a vibrating sample magnetometer (VSM).

Thus, by combining MC computer simulations and analytical approximations for the magnetization, using some physical parameters about the composition and magnetic moment of the CSS, it is possible to reach a better understanding

of their magnetic properties in a wide interval of temperatures. Our main hypothesis is that the main mechanisms of magnetization can be accounted for by considering explicitly the excluded volume interaction, the dipole-dipole interaction between the coated nanoparticles, the external magnetic field, and the anisotropic magnetic contribution.

2. Theoretical background

2.1. Potential model

To carry out the computer simulations of the magnetic CSS, we consider a simplified fluid composed of N spheres of diameter σ (magnetic hard-spheres; MHS) of volume V_i within a volume V at a temperature T. The MHS can be oriented by an external magnetic field B following the Zeeman energy law, since each sphere has an intrinsic dipolar moment μ_i. Therefore, dipole-dipole interactions between MHS should be taken into account. Additionally, the uniaxial anisotropy energy of the CSS is explicitly considered by introducing its magnetic anisotropy constant k_i and the orientation of the anisotropy along the $\hat{k}_i$-axis, *i.e.*, the axis of magnetization, associated with the magnetic moment $\vec{\mu}_i = M_S V_i \hat{m}_i$. The coordinate system and all the vectors involved are depicted in Fig. 1, where $\hat{m}$ and $\hat{h}_i$ are unitary vectors oriented in the directions of the magnetic moment of the particles and the external magnetic field H, respectively.

The Hamiltonian of the dipolar fluid is given by,

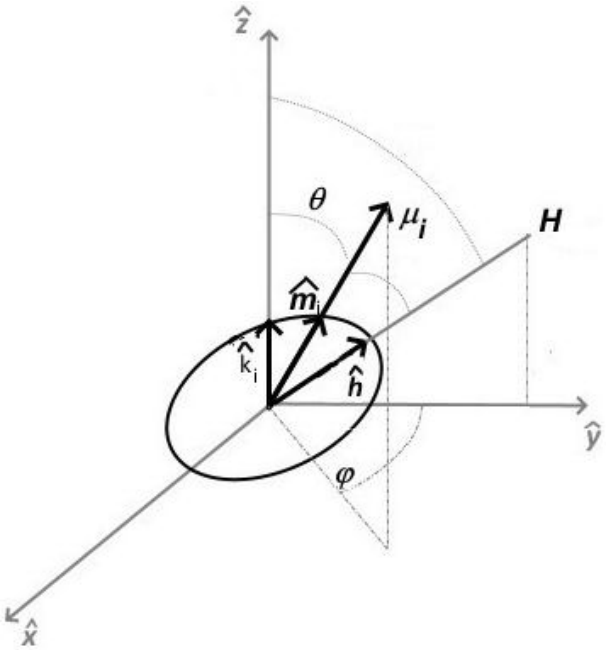

FIGURE 1. The coordinate system and all the vectors and angles with the origin in the geometric center of a CSS.

$$H = K + V_{hs} - \frac{\mu_0}{4\pi}\sum_i \left[\frac{3(\mu_i \cdot r_{ij})(\mu_j \cdot r_{ij})}{|r_{ij}|^5} - \frac{(\mu_i \cdot \mu_j)}{|r_{ij}|^3}\right] - \sum_i \mu_i \cdot B - \sum_i kV_i \left[\hat{k}_i \cdot \hat{m}_i\right]^2, \quad (1)$$

where K is the kinetic energy and V_{hs} represents the typical hard-sphere repulsive interaction at short distances [13].

2.2. Monte Carlo computer simulations

The Monte Carlo computer simulations are carried out in the canonical ensemble with $N = 512$ particles using the standard Metropolis criterion [11] with an acceptance ratio of 30%. 10^6 MC steps are used for equilibration and another 10^6 MC steps to gather statistics; each MC consists of either a displacement or a rotation. In the simulations, the values of B are modified to sweep a set of intensities simulating the operation of a VSM [11,13]. A similar procedure is followed to compute the dependence M *vs* T; $B = \mu_0 H$ is fixed and a sweep of temperatures is programmed; at each temperature, equilibration is reached. Magnetization is computed according to the following Eq. (2), where $< \ldots >$ denotes an ensemble average.

$$\langle \vec{M} \rangle = \sum_{l_1}^{N} \frac{\vec{\mu}_i}{V}. \quad (2)$$

2.3. Analytical approximation

The magnitude of the magnetization of paramagnetic and superparamagnetic MHS with anisotropy energy negligible is well described by the Langevin expression (Eq. (3)), with kB being the Boltzmann constant.

$$M = M_s \left(\coth\left[\frac{\mu_0 \mu H}{k_B T}\right] - \frac{k_B T}{\mu_0 \mu H}\right). \quad (3)$$

Nevertheless, when the anisotropy energy and dipolar contributions of the MHS become significant, the expression for M must be modified. Initially, the dipolar interactions can be expressed in terms of a coupling factor $\lambda = \mu_0 M_s^2 V_i^2 / 4\pi d^3$ [14,15] and the dipolar field $\vec{H}_i^{\text{dip}}$, which is produced by the particles surrounding the ith particle, through Eq. (4).

$$\vec{H}_i^{\text{dip}} = \sum_{i \neq j} \left(\frac{3\hat{r}_{ij}(\hat{m}_j \cdot \hat{r}_{ij}) - \hat{m}_j}{|r_{ij}|^3}\right). \quad (4)$$

Then, the potential energy U weighted with the thermal energy is rewritten as Eq. (5).

$$\frac{U}{k_B T} = -\sum_i \hat{m}_i \cdot \left(\frac{\mu_0 M_s V_i \vec{H}_{\text{ext}}}{k_B T} + \frac{\kappa_i V_i}{k_B T}\hat{k}_i \left[\hat{k}_i \cdot \hat{m}_i\right]\right) - \lambda_\beta \sum_i \hat{m}_i \cdot \hat{H}_i^{\text{dip}}. \quad (5)$$

In Eq. (5), the free (E_{free}) and dipolar coupling (E_{dip}) energy densities are separated as follows in Eq. (6), with $\xi_i = \mu_0 M_s V_i H_{\text{ext}}/k_B T$ and $\alpha_i = \kappa_i V_i/k_B T$.

$$\frac{U}{k_B T} = -\sum_i \hat{m}_i \cdot \left(\xi_i \hat{h} + \alpha_i \hat{k}_i [\hat{k}_i \cdot \hat{m}_i]\right) - \lambda_B \sum_i \hat{m}_i \cdot \vec{H}_i^{\text{dip}} = E_{\text{free}} + E_{\text{dip}}. \quad (6)$$

The component of the magnetization aligned with H can be calculated as the expectation value $\langle M\rangle = \int d\Omega M P$, where the Boltzmann probability distribution P can be expanded (considering weak dipolar interactions) in powers of $\lambda_\beta = \lambda/k_B T$ as $P = P_{\text{free}}(1+\lambda_\beta F(\hat{m}_i))$, where $F(\hat{m}_i)$ is a functional of $\hat{m}_i$. As proposed by Kachkachi *et al.* [16], this allows us to obtain an analytical representation for M in the particular case of a system of interacting particles in the limits of low and high values of H in terms of the free-particle magnetization, $\langle M\rangle_{\text{free}}$, and its derivatives $\partial/\partial\xi\langle M\rangle_{\text{free}}$, as is expressed in Eq. (7), with $A_{ki} = |3(\hat{h}\cdot\hat{r}_{ki})^2 - I|/|r_{ij}|^3$ being the matrix coefficients and the identity matrix I.

$$\langle M\rangle_{\text{dip}} = \langle M\rangle_{\text{free}} + \lambda_\beta \sum_{k=1}^{N} \langle M\rangle_{\text{free}} A_{ki} \frac{\partial}{\partial\xi}\langle M\rangle_{\text{free}}. \quad (7)$$

For the calculation of $\langle M\rangle_{\text{free}}$, it is suitable to take $V_i = V_{\text{mean}}$ as the mean volume of the particle size distribution and also $\kappa_i = \kappa_{\text{mean}}$ corresponds to the mean uniaxial anisotropic constant, allowing the determination of $\langle M\rangle_{\text{free}}$ as the average of the monodisperse ensemble magnetization $\langle M\rangle_{\text{free}}^{\text{mono}}$ over the particle size distribution $f(\sigma_i)$ given by Eq. (8).

$$\langle M\rangle_{\text{free}} = \int f(\sigma)\langle M\rangle_{\text{free}}^{\text{mono}} d\sigma. \quad (8)$$

In the same way, the partition function of a monodisperse system within the canonical ensemble can be calculated in spherical coordinates as

$$Z_{\text{free}} = \int_0^{2\pi}\int_0^{\pi} e^{\alpha\cos^2\theta + \xi\cos\omega}\sin\theta d\theta d\varphi.$$

As shown by several authors [17-19], Z_{free} can be expressed as a single integral (see Eq. (9a) below) in terms of the modified Bessel function of zero-order I_0 for exact numeric calculations, or as a series expansion of Eq. (9b).

$$Z_{\text{free}} = \int_0^{\pi/2} e^{\alpha\cos^2\theta}\cosh(\xi\cos\theta\cos\psi) \times I_0(\xi\sin\theta\sin\psi)\sin\theta d\theta, \quad (9a)$$

$$Z_{\text{free}} = \sum_{n=0}^{\infty}\sum_{n=0}^{\infty}\frac{(n+k)!}{n!(k!)}\left(\frac{-2\alpha}{\xi\cos\psi}\right)^n\left(\frac{\psi\sin^2\psi}{\cos\psi}\right)^k \times \sqrt{\frac{\pi}{2\xi\cos\psi}} I_{n+k+(1/2)}(\xi\cos\psi). \quad (9b)$$

Analyzing the limits of low and high amplitudes of H, it is possible to compute the reduced magnetization of the free particles (corresponding to $f(\sigma_i) = 1$) obtaining Eq. 9(c).

$$\frac{\langle M\rangle_{\text{free}}^{\text{mono}}}{M_s} = \frac{1}{Z_{\text{free}}}\frac{\partial Z_{\text{free}}}{\partial\xi}. \quad (9c)$$

Expanding Eq. (9b) for low and high amplitudes of H, and calculating Eq. (9c) up to second-order in the reduced anisotropy α, and considering $\hat{k}_i$ randomly distributed, one obtains, respectively, the special cases [16-18] for the low field limit given by Eqs. 10(a) and (b), and Eq. (11) for the high field limit.

$$\langle M\rangle_{\text{free}}^{\text{mono}} = M_s\left(\frac{\xi}{3} - \left[1 + \frac{2(2\alpha)^2}{225}\right]\frac{\xi^3}{45}\right); \quad \text{for} \quad 2\sigma < \xi \quad \text{up to} \quad \varepsilon(\alpha^3). \quad (10a)$$

$$\langle M\rangle_{\text{free}}^{\text{mono}} = M_s\left(\frac{\xi}{3} - \left[3 - \frac{8}{3\alpha} - \frac{19}{9\alpha^2}\right]\frac{\xi^3}{45}\right); \quad \text{for} \quad 2\sigma > \xi \quad \text{up to} \quad \varepsilon\left(\left[\frac{\xi}{2\alpha}\right]^3\right). \quad (10b)$$

$$\langle M\rangle_{\text{free}}^{\text{mono}} = M_s\left(1 - \frac{1}{\xi} - \frac{1}{15}\left[\frac{2\alpha}{\xi}\right]\right)^2. \quad (11)$$

With these approximations for $\langle M\rangle_{\text{free}}^{\text{mono}}$, the polydisperse magnetization $\langle M\rangle_{\text{free}}$ can be numerically estimated using Eq. (8), which is used to estimate the total magnetization including dipolar interactions $\langle M\rangle_{\text{dip}}$ according to Eq. (7). The theoretical procedure derived above allows us the progressive description of M in a magnetic fluid, starting with a monodisperse distribution of noninteracting particles, and ending with a more realistic ensemble with size polydispersity and weak dipolar interactions.

2.4. Layer thickness

The thickness Δ of the coating material joined to a spherical nanoparticle (called core) can be estimated by using the known mass ratio of the core and core-shell (m_C/m_{CS}), the diameter of core σ_C, plus the densities of the core ρ_C and shell ρ_S, respectively. This is explained starting with Eq. (12), using the volume ratio of the core and core-shell (V_C/V_{CS}), and including the density of the resultant core-shell sphere ρ_{CS}.

$$\frac{V_C}{V_{CS}} = \frac{m_C}{m_{CS}}\frac{1}{\rho_C}\rho_{CS}. \quad (12)$$

Furthermore, the density ρ_{CS} is related to ρ_C and ρ_S as is described in Eq. (13).

$$\rho_{CS} = \frac{m_{CS}}{V_{CS}} = \frac{m_{CS}}{\frac{m_C}{\rho_C} + \frac{m_S}{\rho_S}} = \frac{m_{CS}\rho_C\rho_S}{m_C\rho_S + m_S\rho_C}. \quad (13)$$

When Eqs. (12) and (13) are combined, it is found an expression containing the mass fractions of the core ($\eta_C = m_C/m_{CS}$) and shell ($\eta_S = m_S/m_{CS}$), which can be determined through thermogravimetric measurements, given by Eq. (14).

$$\frac{V_C}{V_{CS}} = \eta_C \frac{\rho_S}{\eta_C\rho_S + \eta_S\rho_C}. \tag{14}$$

Assuming the spherical shape of the core and core-shell, Eq. (14) can then be reordered and extended including the diameters of both spheres as Eq. (15).

$$\frac{\frac{4\pi}{3}\frac{(\sigma_C+2\Delta)^3}{8}}{\frac{4\pi}{3}\frac{(\sigma_C)^3}{8}} = \left(\eta_C \frac{\rho_S}{\eta_C\rho_S + \eta_S\rho_C}\right)^{-1}. \tag{15}$$

Thus, Δ takes the following mathematical form of Eq. (16).

$$\Delta = \frac{\sigma_C}{2}\left(\left[\frac{\eta_C\rho_S}{\eta_C\rho_S + \eta_S\rho_C}\right]^{-1/3} - 1\right). \tag{16}$$

3. Material and methods

To carry out a comparative analysis between the magnetization obtained experimentally and the one computed via MC computer simulations, the CSS are initially characterized to determine the parameters required by the MC algorithm, such as the inner and outer diameters of the CSS, the concentration, and effective magnetic moment. Then, TEM microscopy experiments, thermogravimetric measurements, and magnetometry are performed. The MNPs were prepared by chemical coprecipitation and the procedure is widely described in a previous experimental report [20]. The CSS obtained are MNPs with a core of magnetite, which are coated with dopamine by ultrasonication. Particle shape and size are analyzed using a TEM JEOL JEM-2100 with FCF-200-Cu grids, where an aliquot dilution 1:100 concentrated at 0.01 mg/ml is dried at room temperature inside of a vacuum chamber. The amount of dopamine covering the core is estimated using a thermogravimetric analyzer TGA Q500 (TA Instruments). Experiments are carried out inside of inert N atmosphere with a flux of 25 ml/min, establishing a heating rate of 10°C/min and covering the interval $40 < T < 850$°C.

To estimate the magnetic moment μCS of an individual CSS, $m_d = 1.4$ mg of dried mass is analyzed by a VSM (VersaLab of Quantum Design). The sample is initially heated at 400 K for 10 min and after that, it is magnetized at room temperature with $H = 2387$ kA/m to determine the total magnetic moment when the sample is magnetically saturated. Additionally, the magnetization of the sample is registered at T = 300 K over the magnetic field amplitude interval $-2387 < H < 2387$ kA/m. To determine κ, the magnetization traces ZFC and FC are measured over the temperature interval $50 < T < 400$ K, using the constant intensity $H = 7.96$ kA/m.

4. Results and discussion

In Fig. 2a), a typical TEM micrograph is shown, where a spherical shape of the CSS is evident. After an analysis of a set of micrographs using the ImageJ software (`https://imagej.nih.gov/ij/`), the relative frequencies of the diameters are computed and displayed in Fig. 2b), leading to a mean particle diameter of $\sigma_C = 13 \pm 5$ nm. Nevertheless, this diameter does not include the thickness of the coating because dopamine was partially o completely evaporated during the TEM measurements. However, the mass of dopamine covering the core is evaporated under controlled conditions during the TGA assay, and Fig. 2c) shows the relative dependence of mass loss on temperature. When the sample is heated up to 800°C, the shell of dopamine is completely evaporated, reaching a total relative amount of 13%. According to Eq. (14), the mass fractions estimated are $\eta_C = 0.87$ and $\eta_S = 0.13$. Then, using the measured σ_C plus the known densities $\rho_C = 5.18$ g/cm^3 and $\rho_S = 1.26$ g/cm^3, the width of the coating computed with Eq. (16) is $\Delta = 1.1$ nm. Thus, the diameter of a CSS is approximately $\sigma_{CS} = \sigma_C + 2\Delta \approx 15 \pm 5$ nm.

According to VSM measurements, the total magnetic moment reached of m_d is $\mu_T = 0.035$ emu (at room temperature

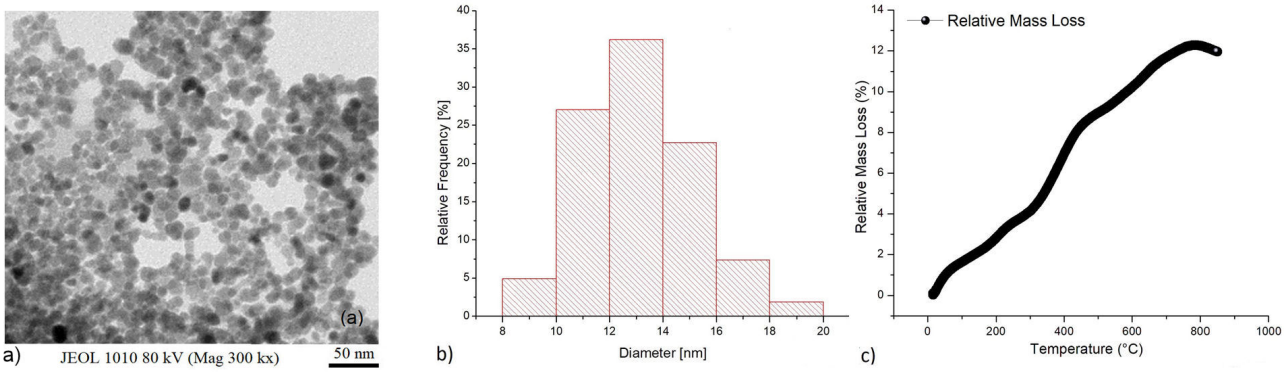

FIGURE 2. a) A typical TEM micrograph of the MNPs, b) the bars plot of the particle diameter distribution, and c) the mass loss dependence with temperature.

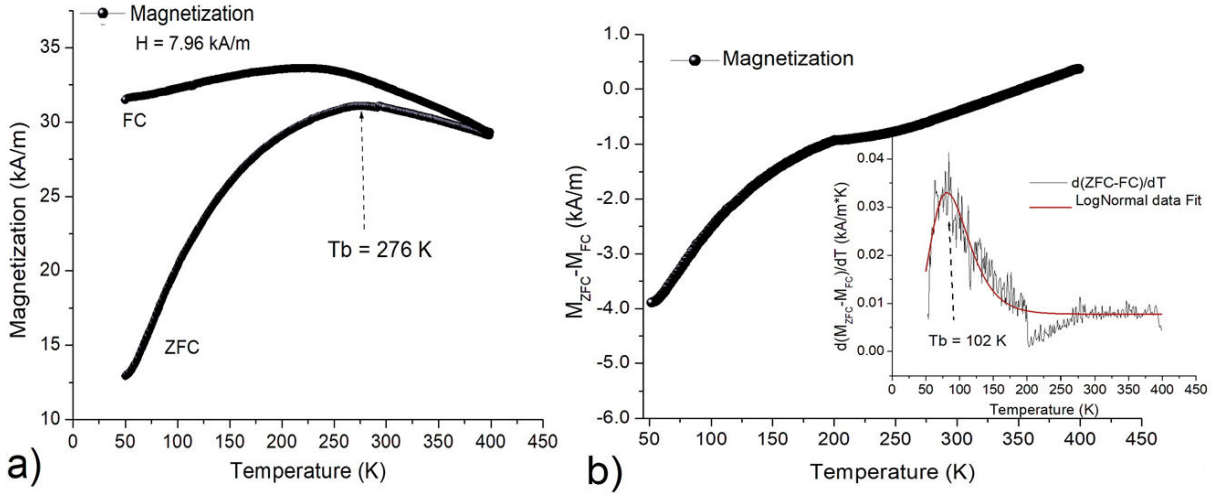

FIGURE 3. a) The dependence M vs T following the ZFC-FC protocol using $H = 7.96$ kA/m; b) the dependence $(M_{ZFC} - M_{FC})$ vs T with the derivative in the inset, plus its corresponding LogNormal fit.

and using $H = 2387$ kA/m). The resulting magnetic moment per CSS $\mu_{CS} = 1.63 \times 10^{-19}$ Am^2 (MKS units) was determined by computing the amount of CSS ($N_{CS} = 2.1 \times 10^{14}$) using the effective mass $m_{CS} = \rho_{CS} * V_{CS} = 6.67 \times 10^{-18}$ g and the ratio $N_{CS} = m_d/m_{CS}$. In the subsequent VSM experiments, the FZF-FC protocol was followed to determine M with $H = 7.96$ kA/m, and the dependence of the magnetization with temperature is plotted in Fig. 3a). In the ZFC trace, the slow growth of M highlights the size polydispersity of the CSS, which is according to the standard deviation of the bars plot displayed in Fig. 2b). The high magnetization observed at 50 K can be associated with a remanent magnetization of the sample because the maximum warming (400 K) was not sufficient to produce a random distribution of the magnetic moments, but the temperature cannot be increased to avoid the evaporation of the organic shell (see Fig. 2c)). Furthermore, the monotonous decreasing of the FC trace below 225 K indicated the importance of the dipolar interactions, which are the main driving force behind the reordering of the magnetic moments in antiparallel orientations to diminish the total magnetization [21]. A careful observation of the maximum M reached in the ZFC trace allows us to get the blocking temperature $Tb = 276$ K. Another alternative to determine Tb is by analyzing the derivative of MZFC - MFC and fitting it using a log-normal regression procedure, as shown in Fig. 3(b), which also allowed us to get the following value $Tb = 102$ K. According to [22], $Tb = 276$ K would be a good representation of the blocking temperature only for a monodisperse ensemble of MNPs, whereas $Tb = 102$ K is a more accurate approximation to the effective blocking temperature for a polydisperse system, like the one depicted by Fig. 2(b). The Néel-Arrhenius law for the magnetic relaxation time τ_N of superparamagnetic materials is given by $\tau_N = \tau_0 e^{\kappa V_C / k_B Tb}$, where $\tau_0 = 1.0$ ns is the constant of the time scale. Then, τ_N coincides with the sampling time of the VSM ($t = 100$ s). Two possible values for the anisotropy constant κ may be associated with the core of the CSS, namely, $\kappa_{102} = 30.6$ kJ/m^3 and $\kappa_{276} = 82.8$ kJ/m^3. Although the ZFC-FC protocol is a useful alternative to determine κ, it is important to highlight that both traces exhibit a nonequilibrium magnetization, because it depends on the magnetic history of the material.

Then, the following experimental parameters are explicitly used in Eq. (1) to carry out the MC computer simulations: $\mu = \mu_{CS}$, $T = 300$ K, $V_i = V_{CS}$, $\kappa = 0$; κ_{102}; κ_{276}, and the interval $-2387 < H < 2387$ kA/m. At the beginning of the simulation, the anisotropy axis of each particle $\hat{k}_i$ is randomly oriented. In Fig. 4(a), three magnetization curves are plotted, which were computed considering each value of κ. Additionally, the experimental one obtained using the VSM is also displayed. For high magnetic fields, all curves appear to be collapsed. In fact, the difference between the experimental magnetic saturation (90 kA/m) and the obtained via MC is up to 1%, showing independence of κ. As can be observed in the inset of Fig. 4(a), for lower magnetic fields things change because the slopes of the curves (initial magnetic susceptibilities) increase when κ diminishes. According to this observation, the magnetization is again computed, but now using $\kappa = \kappa_{102}$ with two different orientations of the anisotropy axis $\hat{k}_i$, the same direction of $\hat{m}_i$ and $\hat{h}_i$, separately. Figure 4b) shows five magnetization curves, one for each orientation of $\hat{k}_i$, also including the random orientation of $\hat{k}_i$, $\kappa = 0$, and the experimental one. As can be seen, all curves are intercepted only in the higher magnetic field and the magnetic saturation has the same value as discussed in Fig. 2a). In the same sense, the parameter χ (see inset of Fig. 4b)) corresponding to $\hat{k}_i$ oriented in the same direction of μ_{CS} and H, is even less than the obtained when $\hat{k}_i$ is randomly oriented. This dependence $\hat{k}_i$ vs χ was previously reported in Ref. [13].

The dependence of the magnetization on the temperature is discussed now. The temperature interval in the VSM exper-

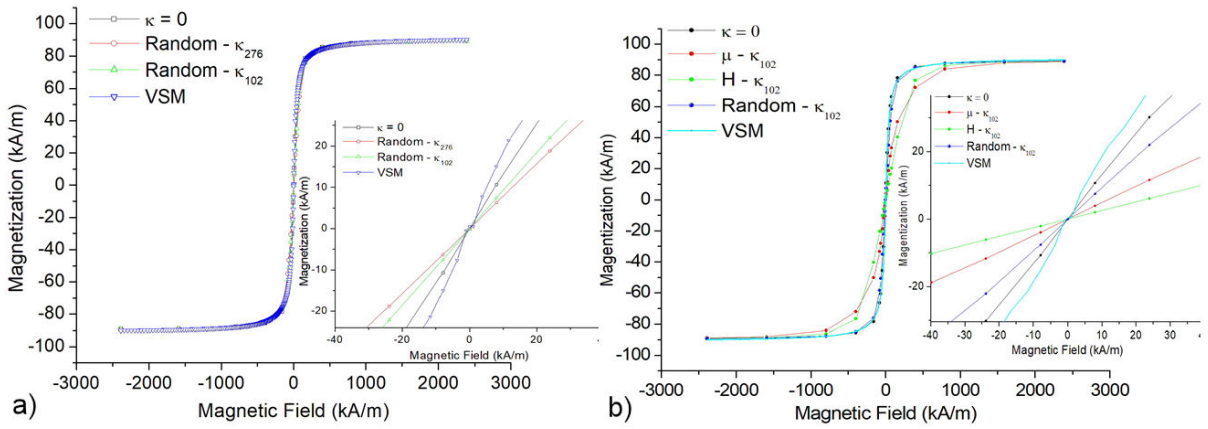

FIGURE 4. Dependences M vs H considering: a) $\kappa = 0$, $\kappa 102$ and $\kappa 276$; with randomly oriented, plus the experimental plot obtained via VSM; b) $\kappa = 0$, $\kappa 102$; with oriented in the directions $\hat{m}_i$, $\hat{h}_i$ and random, plus the experimental plot. The slopes of the lines in the insets represent the magnetic susceptibilities.

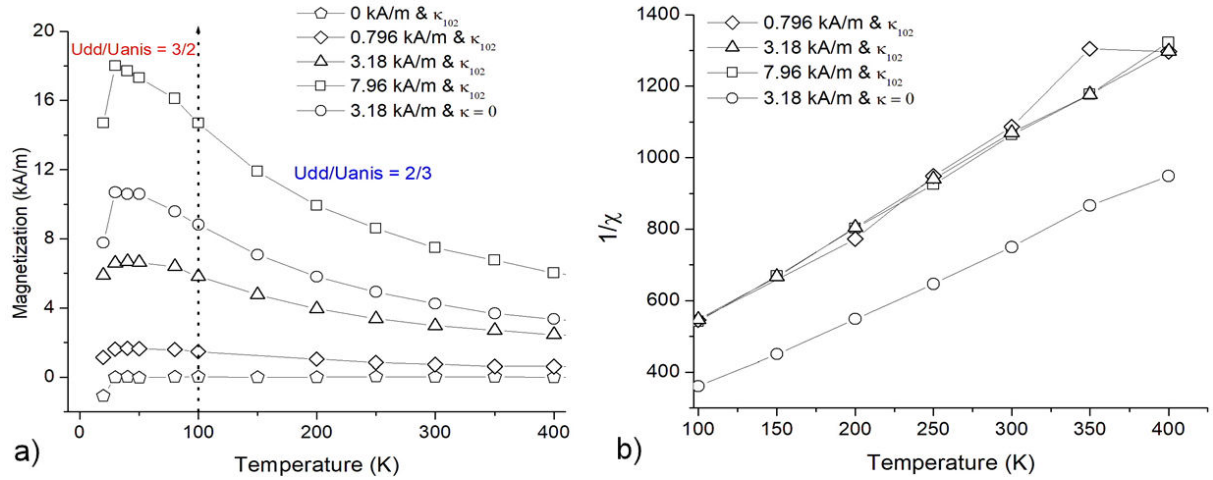

FIGURE 5. a) The dependences M vs T obtained via MC with different magnetic field intensities, $\kappa = \kappa 102$, and $\kappa = 0$ plotted in the interval $20 < T < 400$ K. b) The dependence $1/\chi$ vs T in the interval $100 < T < 400$ K.

iment was $50 < T < 400$ K, whereas in the MC simulation, it is not limited. In Fig. 5a), the curves for weak magnetic intensities, namely, $H = 0$, 0.796, 3.18 (with $\kappa = 0$, $\kappa = \kappa_{102}$) and 7.96 kA/m are shown. As the acceptance rate of the MC simulation is drastically decreased below 20 K, we have restricted the analysis to the interval $20 < T < 400$ K. In all curves, the magnetizations reached maximum values between 30 K and 40 K and suffers a significant decrease at 20 K. Above 100 K, all curves (except $H = 0$ kA/m) satisfy the Curie law, as can be observed in the corresponding plots $1/\chi$ vs T of Fig. 5b); all points almost collapse in a straight line. When $\kappa = 0$, it is found the lower slope ($< 45\%$) because the magnetic susceptibility χ has reached the highest value, showing a good agreement with the magnetization curve of Figs. 4a) and b). When the amplitude of H is very weak, the main contribution to the energy of the MHS is provided by the dipolar interactions Udd and the anisotropy energy $Uanis$. Further analysis of the rate $Udd/Uanis$ exhibits $Udd/Uanis \approx 2/3$ above 100 K and below $Udd/Uanis \approx 3/2$. This last behavior agrees with the observations of the dipolar interactions in the FC trace of the magnetization obtained in Ref. [21].

To highlight the importance of the dipolar interactions at low temperatures, in Fig. 6 configurations of the MHS (magnetized with $H = 7.96$ kA/m) are shown for two different temperatures, namely, 100 K and 20 K. The spheres are placed in the corresponding spatial positions and the arrows describe the orientation of the magnetic moments. As can be observed in the XYZ view and the XY projection, the orientations at 100 K have some random distribution. The opposite behavior is observed at 20 K, where the magnetic moments are aligned perpendicularly to $\hat{z}$, arranging planes antiparallel oriented like an "antiferromagnetic or ferrimagnetic domain".

A discussion about the theoretical models for M applied to the experimental (M_{VSM}) and the simulated curve ($M_{\kappa 102}$) when $\hat{k}_i$ is randomly oriented is conducted now. For this purpose, M_{VSM} and $M_{\kappa 102}$ are plotted with the corre-

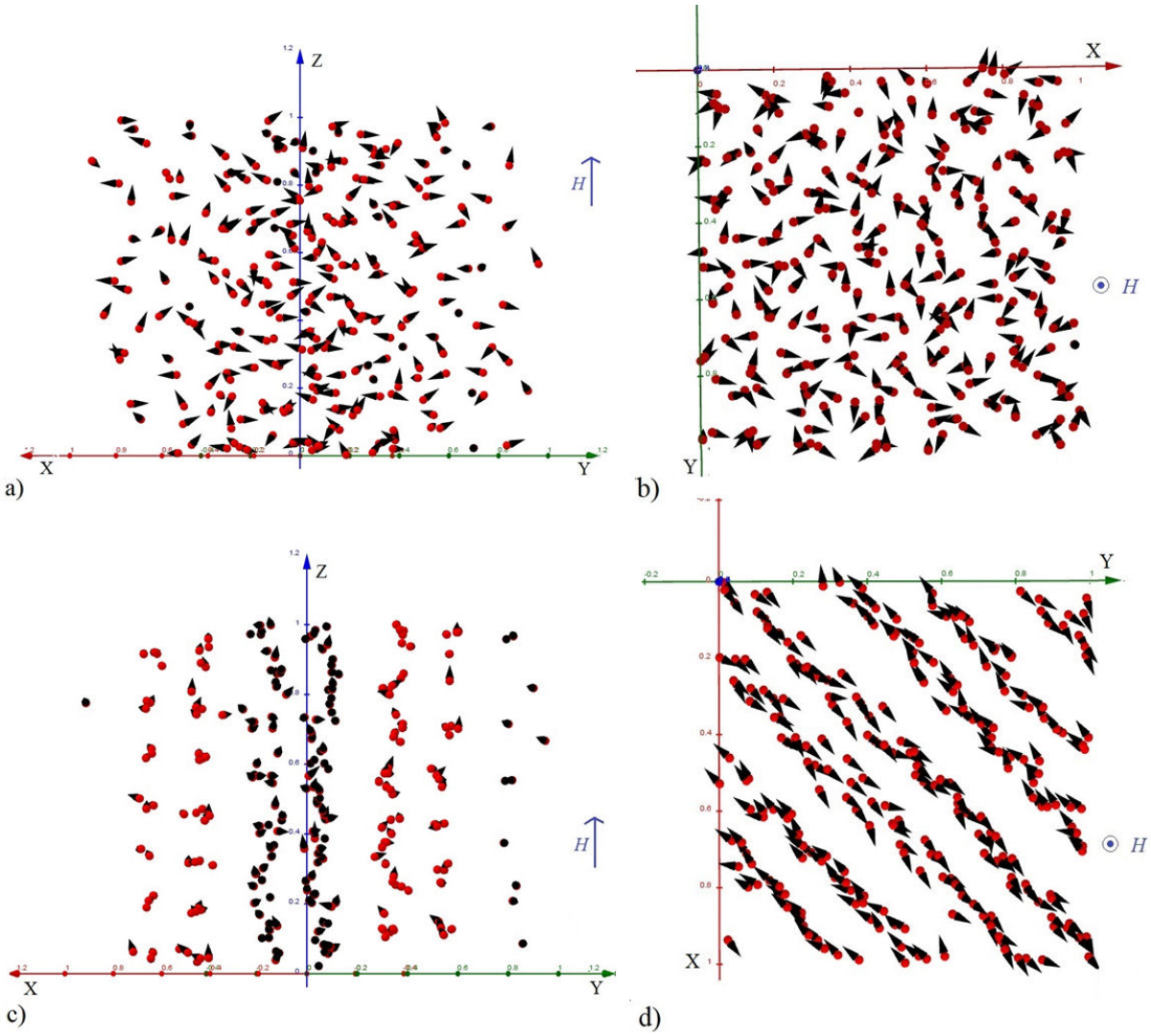

FIGURE 6. Thermalized configurations of the MHS inside of the simulation box in isometric views XYZ and the respective XY projections applying $H = 7.96$ kA/m $\hat{z}$: at a), b) 100 K and at c), d) 20 K.

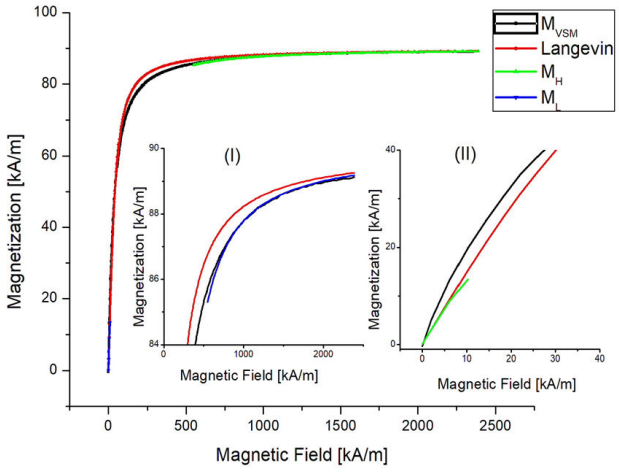

FIGURE 7. Magnetization M_{VSM} superimposed with the corresponding Langevin equation (Eq. (3)), including M_H (inset I) and M_L (inset II).

sponding Langevin magnetization (see Eq. (3)). Also, the magnetization approximated for low (M_L) and high (M_H) fields with Eqs. (10) and (11), respectively, are included. Starting with M_{VSM}, Fig. 7 shows a full-scale view of this qualitative comparison. As can be expected for a sample mainly superparamagnetic, the difference between the M_{VSM} and the Langevin equation is only perceptible in the inflection range of H, that is, where the linear response fails and the sample became saturated. However, the inset (I) in Fig. 7 shows a close-up in the high field region ($H > 2\kappa/\mu_0 M_s$), where M_H predicts more accurately the real magnetization M_{VSM}. Inset (II) in Fig. 7 also shows a close-up with M_L, where M_{VSM} has a greater slope than even the Langevin equation. This suggests the existence of an interval where the dipolar interactions could be of significance, or probably a little fraction of CSS has the anisotropy axis aligned to H rather than randomly distributed.

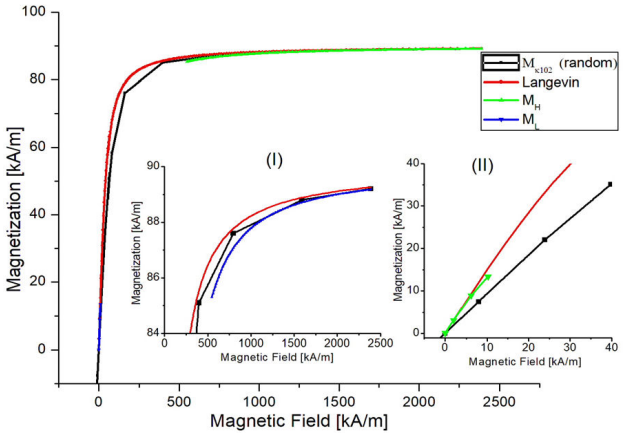

FIGURE 8. Magnetization $M_{\kappa 102}$ superimposed with the corresponding Langevin equation (Eq. (3)), including MH (inset I) and ML (inset II).

Figure 8 shows the same qualitative analysis on $M_{\kappa 102}$ as in Fig. 7. In the full scale of H, the Langevin model again differs only near the transition to magnetic saturation. Nevertheless, inset (I) of Fig. 8 shows M_H with a better agreement with M_{VSM}. Moreover, in the inset (II) of Fig. 8, M_L remains under the Langevin limit, even when the simulation has taken into account the dipolar interactions. This reinforces the idea that the initial slop of the experimental curve provided in the inset of Fig. 7 must be due to the presence of a fraction of particles where the anisotropy axis is aligned with the external field.

5. Conclusions

A detailed characterization of a magnetite-dopamine core-shell nanoparticle sample was presented, including direct measurement of particle size through TEM microscopy, the thickness of coating using TGA, the blocking temperature and M vs H response, by vibrating sample magnetometry. Using those measurements, the parameters needed to carry out MC computer simulations were obtained. The dependence of H on the magnetization was studied by Monte Carlo computer simulations, using two possible magnetic anisotropy constants and three different orientations of the anisotropy axis $\hat{k}_i$. As was observed, when the CSS have $\kappa_{102} = 30.6$ kJ/m^3 with $\hat{k}_i$ randomly oriented, the simulation predicted an M vs H dependence more similar to the experimentally measured and fitted to an ideal Langevin equation. Additionally, it was demonstrated that the correlation of the magnetization with H can be improved (in the limits of high and weak amplitudes of H) when the anisotropy contributions are explicitly taken into account. Furthermore, the dependence of T on the magnetization estimated by MC exhibited the non-compliance of the Curie law below $T = 100$ K, which almost coincides with the minimum $Tb = 102$ K measured. At these temperatures, the dipolar interactions mainly contributed to the total energy of the ensemble and the CSS adopted an ordered orientation even when the magnetic field was null.

Last, but not least, we should point out that this work also provided a condensed derivation of the magnetization including different physical contributions, which might be implemented in further works to properly analyze the magnetization beyond the ideal Langevin equation.

Acknowledgments

Authors want to thank CONACYT-FORDECYT-PRONACES for financially supporting this work (Grant No. 568483/2020 “Frontera de la Ciencia”). Authors also thank Christopher E. Trent for carefully reviewing the language of the manuscript.

1. R. Eivazzadeh-Keihan *et al.*, A novel biocompatible core-shell magnetic nanocomposite based on cross-linked chitosan hydrogels for in vitro hyperthermia of cancer therapy, *International journal of biological macromolecules* **140** (2019) 407. https://doi.org/10.1016/j.ijbiomac.2019.08.031.

2. S. Wu *et al.*, Fe3O4 magnetic nanoparticles synthesis from tailings by ultrasonic chemical co-precipitation, *Materials Letters* **65** (2011) 1882. https://doi.org/10.1016/j.matlet.2011.03.065.

3. F. Zhao, B. Zhang, and L. Feng, Preparation and magnetic properties of magnetite nanoparticles, *Materials Letters* **68** (2012) 112. https://doi.org/10.1016/j.matlet.2011.09.116.

4. A. K. Ebrahimi, M. Barani, and I. Sheikhshoaie, Fabrication of a new superparamagnetic metal-organic framework with core-shell nanocomposite structures: Characterization, biocompatibility, and drug release study, *Materials Science and Engineering: C.* **92** (2018) 349. https://doi.org/10.1016/j.msec.2018.07.010.

5. M. Woińska *et al.*, Magnetic interactions in an ensemble of cubic nanoparticles: A Monte Carlo Study, *Physical Review B.* **88** (2013) 144421. https://doi.org/10.1103/PhysRevB.88.144421.

6. L. Néel, Antiferromagnetism and Ferrimagnetism, *Proc. Phys. Soc. A* **65** (1952) 869. https://doi.org/10.1088/0370-1298/65/11/301.

7. J. S. Smart and The Néel theory of ferrimagnetism, *American Journal of Physics* **23** (1955) 356. https://doi.org/10.1119/1.1934006.

8. A. K. Murtazaev, M. K. Ramazanov, and M. K. Badiev, Phase transitions and critical phenomena in the antiferromagnetic Ising model on a layered triangular lattice, *Physica A: Statistical Mechanics and its Applications* **507** (2018) 210. https://doi.org/10.1016/j.physa.2018.04.106.

9. A. Zaim, and M. Kerouad, Monte Carlo simulation of the compensation and critical behaviors of a ferrimagnetic core/shell nanoparticle Ising model, *Physica A: Statistical Mechanics and its Applications* **389** (2010) 3435. https://doi.org/10.1016/j.physa.2010.04.034.

10. T. Preis, P. Virnau, W. Paul, and J.J. Schneider, GPU accelerated Monte Carlo simulation of the 2D and 3D Ising model, *Journal of Computational Physics* **228** (2009) 4468. https://doi.org/10.1016/j.jcp.2009.03.018.

11. M. E. Cano *et al*., *Magnetic Properties of Synthetic Eumelanin-Preliminary Results*, **84** (2008) 627. https://doi.org/10.1111/j.1751-1097.2008.00302.x.

12. P. Coutiño, N. Ibarra-ávalos, A. Gil-Villegas, Phase transitions of granular disks with a magnetic dipole, *Rev. Mex. Fis.* **56** (2010) 435. http://revistas.unam.mx/index.php/rmf/article/view/23508.

13. J. Londoño-Navarro, J.C. Riaño-Rojas, E. Restrepo-Parra, Competition between anisotropy and dipolar interaction in multicore nanoparticles: Monte Carlo simulation, *Dyna* **82** (2015) 66. http://dx.doi.org/10.15446/dyna.v82n194.44297.

14. A. A. Kuznetsov and A. F. Pshenichnikov, Sedimentation equilibrium of magnetic nanoparticles with strong dipole-dipole interactions, *Physical Review E* **95** (2017) 032609. https://doi.org/10.1103/PhysRevE.95.032609.

15. P. E. Jönsson and J. L. Garcia-Palacios, Thermodynamic perturbation theory for dipolar superparamagnets, *Physical Review B* **64** (2001) 174416. https://doi.org/10.1103/PhysRevB.64.174416.

16. H. Kachkachi and M. Azeggagh, Magnetization of nanomagnet assemblies: Effects of anisotropy and dipolar interactions, *The European Physical Journal B-Condensed Matter and Complex Systems* **44** (2005) 299. https://doi.org/10.1140/epjb/e2005-00129-0.

17. M. Respaud, Magnetization process of noninteracting ferromagnetic cobalt nanoparticles in the superparamagnetic regime: Deviation from Langevin law, *Journal of applied physics* **86** (1999) 556. https://doi.org/10.1063/1.370765.

18. P.J. Cregg and L. Bessais, Series expansions for the magnetisation of a solid superparamagnetic system of non-interacting particles with anisotropy, *Journal of magnetism and magnetic materials* **202** (1999) 554. https://doi.org/10.1016/S0304-8853(99)00422-9.

19. P.J. Cregg and L. Bessais, A single integral expression for the magnetisation of a textured superparamagnetic system, *Journal of magnetism and magnetic materials* **203** (1999) 265. https://doi.org/10.1016/S0304-8853(99)00269-3.

20. O. Cervantes *et al*., An easily prepared ferrofluid with high power absorption density and low cytotoxicity for biomedical applications, *Materials Chemistry and Physics* **245** (2020) 122752. https://doi.org/10.1016/j.matchemphys.2020.122752.

21. P. Guardia *et al*., Surfactant effects in magnetite nanoparticles of controlled size, *Journal of Magnetism and Magnetic Materials* **316** (2007) e756. https://doi.org/10.1016/j.jmmm.2007.03.085.

22. I.J. Bruvera *et al*., Determination of the blocking temperature of magnetic nanoparticles: The good, the bad, and the ugly, *Journal of Applied Physics* **118** (2015) 184304, https://dx.doi.org/10.1063/1.4935484.